

Supporting Information

Dynamically Imaging Collision Electrochemistry of Single Electrochemiluminescence Nano-Emitters

Cheng Ma, Wanwan Wu, Lingling Li, Shaojun Wu, Jianrong Zhang, Zixuan Chen*
and Jun-Jie Zhu*

State Key Laboratory of Analytical Chemistry for Life Science, School of Chemistry
and Chemical Engineering, Nanjing University, 163 Xianlin Ave, Nanjing 210023,
China

Corresponding Authors: Zixuan Chen and Jun-Jie Zhu

Email: chenzixuan@nju.edu.cn and jjzhu@nju.edu.cn

Table of contents

1. Electrochemiluminescence (ECL) coupled with photoluminescence (PL) microscopy set-up
2. Co-localization analyses of ECL images and SEM images
3. ECL reaction kinetics of individual nanoparticles
 - ECL reaction mechanisms of individual RuDSNs
 - Relationship between ECL reaction kinetics and the nature of electrode surface
4. ECL emission on the cell upper surface
5. Stochastic collision nanoelectrochemistry
 - Random walk of single nanoparticle in the electrode vicinity
 - Horizontal moving trajectory in the collision process
 - The different surface modification of nanoparticles and electrodes for studying sticking collision probability
 - Spatial distribution of collision intensity and frequency across GC electrode surface
 - ECL intensity distribution of statistic sticking collision events in the CCD-view
 - Relay probe based on successive collision events
6. COMSOL simulation for sub-particle ECL pattern analysis
 - Reactions and parameters for digital simulation
 - Subdomain setting
 - Physical fields
 - Meshes settings
 - Simulation results
7. Experimental section
 - Chemicals and general techniques
 - Preparation and characterization of RuDSNs and RuCSPs
8. Description of the movies
9. References

1. Electrochemiluminescence (ECL) coupled with photoluminescence (PL) microscopy set-up.

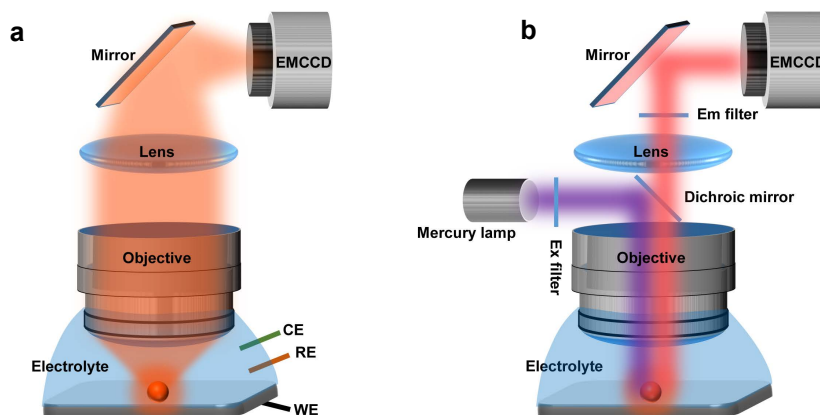


Figure S1. (a) Schematic illustration of the ECL microscopy setup. Application of a voltage to the work electrode resulted in the ECL emission of RuDSNs, which was collected by a water-immersion objective of high numerical aperture. The diverging light was focused by the imaging lens and then was imaged on the EMCCD. (b) Schematic illustration of the PL microscopy setup, which was established based on the ECL microscope with a light source and filters. The setup used a white light source (mercury lamp) and an Ex filter for excitation light generation. A dichroic mirror was used to prevent the excitation light from entering the camera. The PL of RuDSNs penetrated an Em filter and then was imaged on the EMCCD.

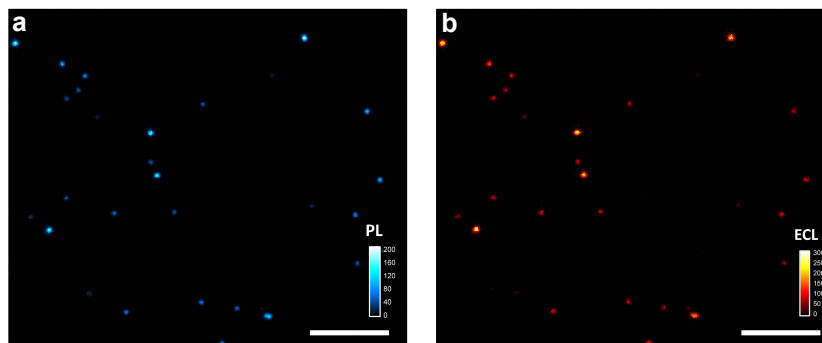


Figure S2. Co-localization of the PL image and the ECL image of a same set of RuDSNs. (a) The PL image of the RuDSNs on the GC electrode. (b) The corresponding ECL image of the same set of RuDSNs. The potential was cyclically scanned from 0 to 1.4 V (vs. Ag/AgCl reference electrode) at a scan rate of 100 mV/s. The exposure time of EMCCD was 1 s for ECL and PL imaging. Scale bars (white), 20 μ m.

2. Co-localization analyses of ECL images and SEM images.

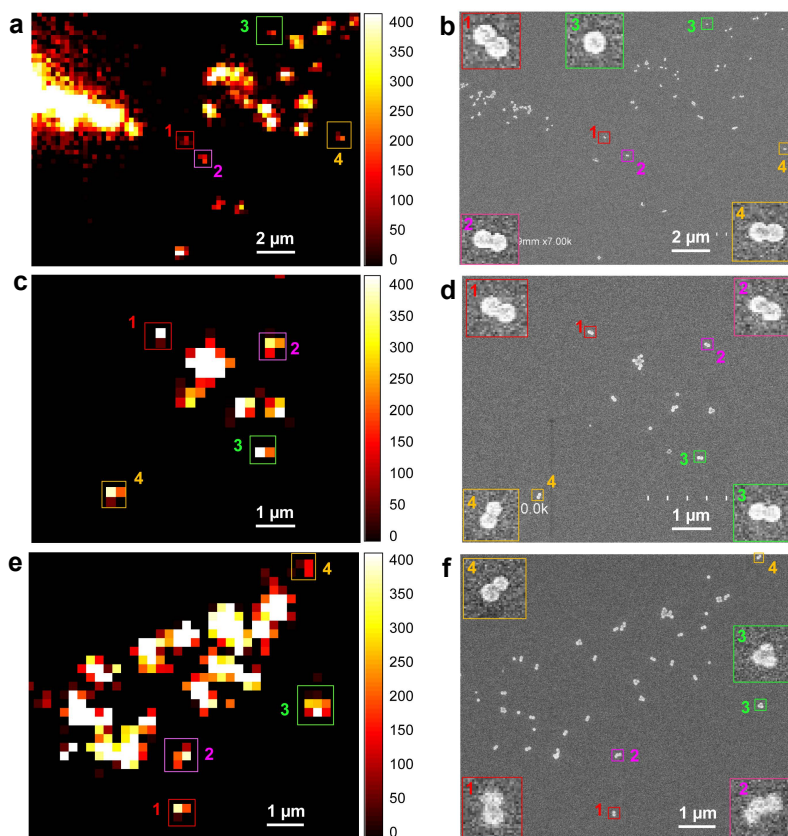
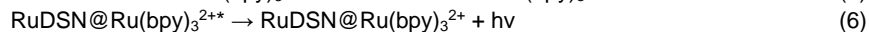
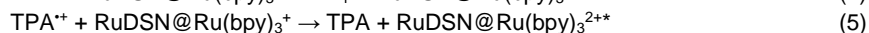


Figure S3. (a,c,e) Typical zoom-in ECL images of the RuDSNs on the GC electrode surface. The potential was cyclically scanned from 0 to 1.4 V (vs. Ag/AgCl reference electrode) at a scan rate of 100 mV/s. The exposure time of EMCCD was 1 s. (b,d,f) The corresponding SEM images of the same set of particles as in (a,c,e). Insets showed the detailed morphologies of RuDSNs numbered with 1-4.

3. ECL reaction kinetics of individual nanoparticles

ECL reaction mechanisms of individual RuDSNs: As shown in Figure 2, when the electrode potential was scanned beyond 0.7 V, the enhancement of the oxidation current suggested that the direct oxidation of coreactant TPA occurred,^[1] which was confirmed by the controlled trials (Figure S4). Then, the initial ECL signal started following the oxidation of TPA and reached a maximum at 0.87 V. It should be pointed out that the potential of this ECL peak was too negative to directly oxidize RuDSN@Ru(bpy)₃²⁺ to RuDSN@Ru(bpy)₃³⁺, which can be further reduced by TPA free radicals to form emitter RuDSN@Ru(bpy)₃^{2+*}. The ECL signal that was observed herein was attributed to the “revisited” route involving both TPA cation radicals (TPA⁺) and TPA free radicals (TPA^{*}):^[2]



Where TPAH⁺ is Pr₃NH⁺, TPA⁺ is Pr₃N⁺, TPA^{*} is Pr₂NC^{*}HCH₂CH₃, P₁ is Pr₂N⁺=CHCH₂CH₃.

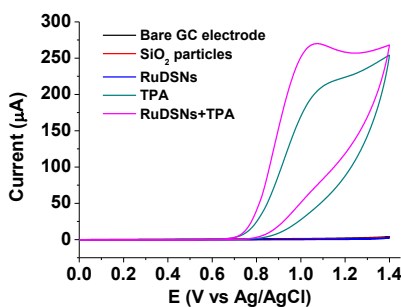


Figure S4. CV curves of bare GC electrode (black line), GC electrode immobilized by either silica nanoparticles (red line) or RuDSNs (blue line) in PBS buffer, and bare GC electrode (green line) and GC electrode immobilized by RuDSNs (purple line) in PBS buffer containing 100 mM TPA coreactant. The potential was cyclically scanned from 0 to 1.4 V at a scan rate of 20 mV/s.

As the potential continues to scan beyond 0.87 V, the ECL intensity of the nanoparticles starts to decrease, although the oxidation current increases and then reaches a peak at 1.05 V. The contravention between the ECL emission intensity and the oxidation current is attributed to direct anodic oxidation of TPA[•] at the electrode interface.^[1, 3] It is noteworthy that we observe a small ECL peak at 1.19 V. It derives from the direct oxidation of Ru(bpy)₃²⁺ inside the nanoparticle based on the electron tunnelling/hopping mechanism,^[4] which is consistent with the oxidation current of Ru(bpy)₃²⁺ (Figure S5). This phenomenon is supported by the numerical simulated result reported by Paolucci and co-workers.^[2a]



This is the first time that the ECL emission by the electron tunnelling and hopping mechanism at single-nanoparticle level is observed, although the “revisited” route is verified by imaging the ECL profile in single microbeads as well as SECM-ECL experiments.^[2b, 2c] It is noteworthy that the ECL-potential curve can accurately reveal specific electrochemical reaction without the interference from the charge-discharge current, side reactions and water decomposition reaction, which are inevitable in traditional CV measurements. In addition, as illustrated in Figure 2m, the ECL-potential curve shows a zero background signal from the blank electrode substrate during the entire ECL process, which demonstrates the high accuracy and sensitivity for imaging local electrochemical reactions by our ECL microscopy.

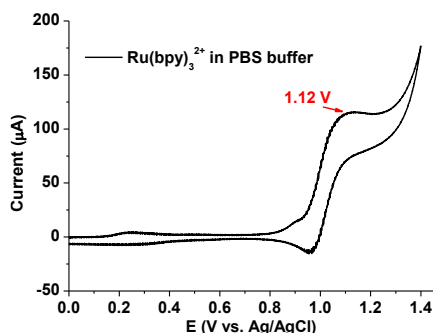


Figure S5. CV curve of 400 µM Ru(bpy)₃²⁺ in 100 mM PBS buffer. Work electrode: GC electrode. The potential is cyclically scanned from 0 to 1.4 V at a scan rate of 100 mV/s.

Relationship between ECL reaction kinetics and the nature of electrode surface: A crucial point in the efficiency of the ECL generation is the chemical and physical state of the electrode surface where the ECL process is initiated.

To investigate the ECL behaviour of individual RuDSNs on different electrode interface, we compare the ECL peak voltages and intensities of single RuDSNs on the bare GC electrode, the bare gold electrode, and the gold electrode blocked by bovine serum albumin (BSA). To verify the blockage effect, we measure electrochemical impedance spectroscopy (EIS) and CV of the gold electrode before and after blocked by BSA (Figure S6a,b). Both the enhanced impedance and the decreasing current confirm that BSA (1mg/mL) can block the active sites of the gold electrode surface. As a consequence, individual RuDSNs on these three electrodes show different ECL-potential curves (Figure S6c), such as peak voltage and intensity, which suggest the essential role of electrode materials and interfacial impedance in ECL reaction kinetics. The statistics (Figure S6d,e) show more negative ECL peak voltage of individual RuDSNs on the gold electrode than on the GC electrode, because gold materials are known to be able to enhance the oxidation of TPA and generation of ECL from RuDSNs. But the growth of surface gold oxide leads to the decrease of TPA oxidation rate and thus decline of the ECL intensity at the high potential. In addition, the strong nonspecific adsorption of BSA on the gold electrode increases the electrochemical impedance and inhibits the interfacial electron transfer, leading to a suppressed ECL intensity and ECL peak shifting toward more positive voltage (Figure S6f).

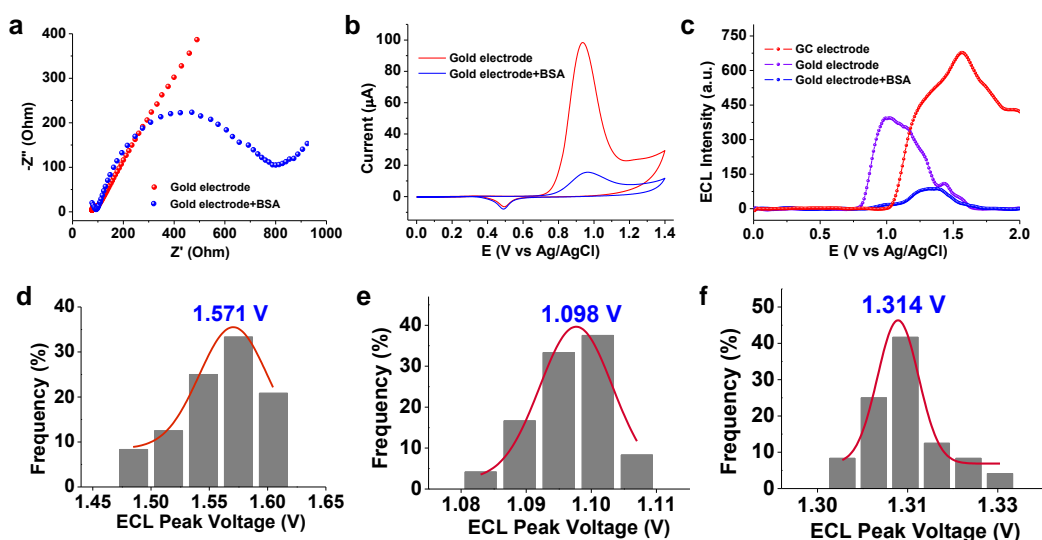


Figure S6. (a) Electrochemical impedance spectroscopy (EIS) and (b) oxidation current of TPA at the bare gold electrode before and after blocked by BSA. (c) Typical ECL intensity curves of single RuDSNs with linear sweep voltammetry using different work electrodes: Bare GC electrode, bare gold electrode, and gold electrode blocked by BSA, respectively. (d-f) The distribution of the ECL peak voltage of individual RuDSNs with linear sweep voltammetry using different work electrodes: (d) bare GC electrode, (e) bare gold electrode, and (f) gold electrode blocked by BSA. The potential is scanned from 0 to 2 V at a scan rate of 10 mV/s in 200 mM PBS buffer containing 100 mM TPA. The exposure time of EMCCD is 1 s.

4. ECL emission on the cell upper surface.

A HeLa cell line was purchased from the Institute of Cell Biology at the Chinese Academy of Sciences (Shanghai, P. R. China) and cultured in HDMEM (Life Technologies, Grand Island, NY, USA) containing 10% fetal bovine serum, 100 U/mL penicillin and 100 μ g/mL streptomycin at 37 $^{\circ}$ C under 5% CO₂ atmosphere. At the logarithmic growth phase, the cells suspension were transferred at a GC electrode surface and left undisturbed for 8 h for cells adherence. The smooth surface of GC electrode allowed HeLa cells to adhere to and grow on it.

According to our simulated results (Figure 3n) and eq. (1-6), RuDSNs can emit ECL far from the electrode surface by the “revisited” mechanism. In order to demonstrate this, we investigated the ECL emission of RuDSNs on the upper surface of HeLa cells. The previous report demonstrated the height of the cell upper surface is 1–2 μ m.^[2d] However, the electron blocking effect of insulating proteins and cells dramatically suppressed the ECL emission. Thus, to perform the ECL imaging on the upper surface of cells, we synthesized 500 nm RuDSNs for higher ECL intensity.

To perform cell experiment, we first placed HeLa cells on the GC electrode surface, and then deposited RuDSNs on the cell upper surface. In detail, the adherent HeLa cells were incubated with RuDSNs for 20 min in the culture medium. During this period, RuDSNs adhered to the cell upper surface by nonspecific absorption. After replacing the culture medium with PBS buffer that contained 100 mM TPA as coreactant, the PL imaging and ECL imaging were performed. As illustrated in Figure S7, the bright field and PL images showed several RuDSNs on the upper surface of single HeLa cell. Because of the complex topography of the cell upper surface, the RuDSN on the focus plane (cell center region, marked with 1 in Figure S7b) displayed brighter PL intensity than the other on the defocus plane (cell edge region, marked with 2 in Figure S7b). For ECL imaging, the potential was cyclically scanned from 0 V to 1.8 V, and we observed that both the particles on the upper surface of HeLa cells can emit bright ECL (Figure S7c). The ECL mechanism was attributed to both the reductive radical TPA^\cdot and oxidative radical cation $\text{TPA}^{+\cdot}$ diffusing into micrometric distances from the electrode surface and generating ECL on the cell upper surface.^[2d] Although the concentration of radical cation $\text{TPA}^{+\cdot}$ dramatically reduced with the increasing distance from the electrode, the highly dense $\text{Ru}(\text{bpy})_3^{2+}$ -doping particles offered more sufficient ECL emission than single $\text{Ru}(\text{bpy})_3^{2+}$ dye.

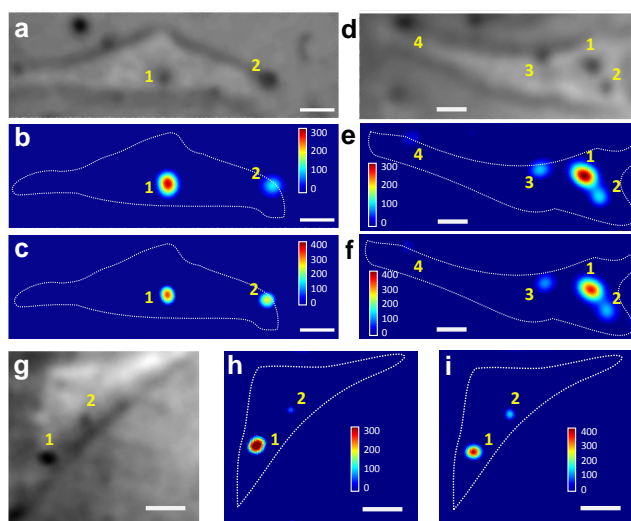


Figure S7. Three groups of ECL imaging of RuDSNs on the upper surface of HeLa cell. The bright field (a,d,g), PL images (b,e,h), and ECL images (c,f,i) of RuDSNs on the cell upper surface. The RuDSNs marked with 1-4 represent the RuDSNs on the cell upper surface. The potential is scanned from 0 to 1.8 V at a scan rate of 100 mV/s. Exposure time: 1 s. Scale bars (white), 10 μm .

5. Stochastic collision nanoelectrochemistry

Random walk of single nanoparticle in the electrode vicinity: The ECL microscopy enables us to directly observe diverse collision dynamics. As shown in Figure S8, we noticed that consecutive ECL spots burst in a same region, which suggested rebound behaviour during the collision process. These results demonstrated that once a RuDSN diffused to the vicinity of the electrode, it would undergo multiple collisions with the electrode. A bunching of collisions implied the random walk of single RuDSNs in the vicinity of electrode surface.

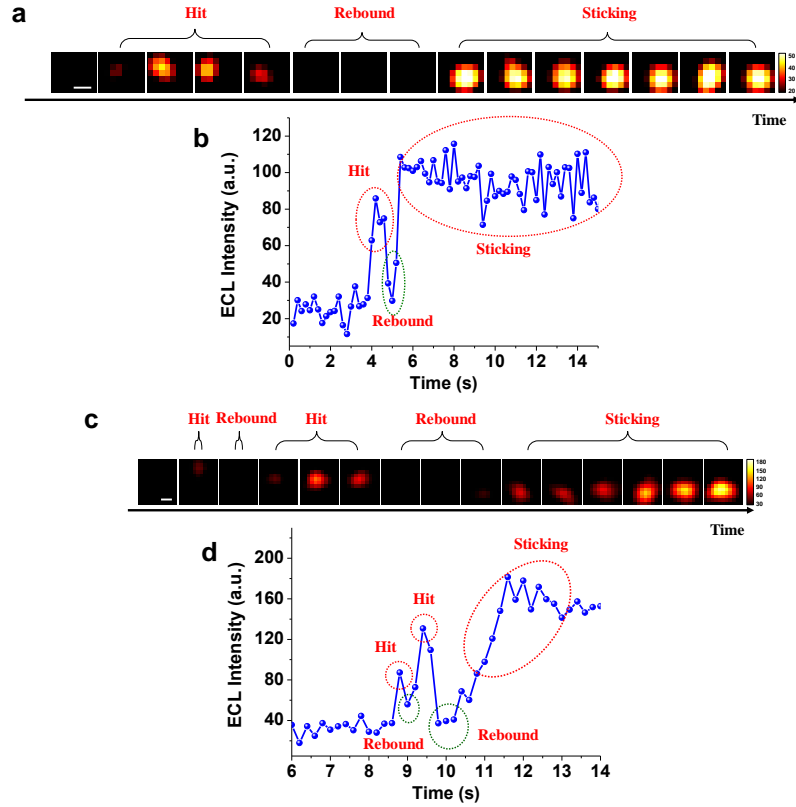


Figure S8. (a,c) Successive snapshots of ECL bursts in a same region. (b,d) ECL intensity vs time elapse in the local region (a,c) of the GC electrode. The interval of each image: 200 ms/frame. Scale bars (white), 1 μm .

Horizontal moving trajectory in the collision process: Time-elapse ECL snapshots illustrated that single RuDSN also had a horizontal movement during the collision process. The horizontal position of the RuDSN was located by fitting its diffraction-limited emission by a 2D Gaussian model:

$$I(x, y) = z_0 + I_0 \exp \left\{ -\frac{1}{2} \left[\left(\frac{x-x_0}{s_x} \right)^2 + \left(\frac{y-y_0}{s_y} \right)^2 \right] \right\} \quad (10)$$

where, $I(x, y)$ represents the measured diffraction-limited emission across the x, y pixels of the CCD; z_0 is the background intensity; I_0 is the peak emission intensity; s_x and s_y are the width of the distribution in x and y , respectively; x_0 and y_0 indicate the location of the maximum intensity distribution and thus the position of the nanoparticle. These dynamic behaviours revealed the random Brownian motion of single nanoparticles during the collision process (Figure S9).

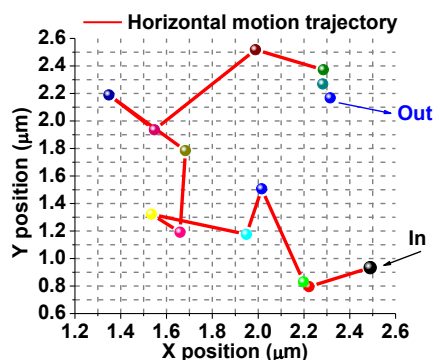


Figure S9. The horizontal moving trajectory of single RuDSN in an elastic collision process.

The different surface modifications of nanoparticles and electrodes for studying sticking collision probability: For bare RuDSNs, the ECL intensity often showed staircase signals with the time trajectory, suggesting strong adsorption effect between RuDSNs and the GC electrode surface. We assumed that collision types depended on the physical and chemical states of both particles and electrodes, e.g. particular structural defects on the electrode surface or places with surface adsorbates that promoted adsorption of the nanoparticles. To study factors affecting the probability of nanoparticle sticking collisions, we coated the RuDSNs with BSA, poly(sodium 4-styrenesulfonate) (PSS), and poly(allylamine hydrochloride) (PAH), respectively (Figure S10). The zeta potential of RuDSNs in 200 mM PBS (pH = 7.0) was 16.6 ± 3.7 (Figure S10a), which was attributed to a large number of positively charged $\text{Ru}(\text{bpy})_3^{2+}$ on the surface of RuDSNs. However, after surface modification of BSA, due to the low isoelectric point of BSA ($pI = 4.7$), RuDSNs@BSA showed a negative potential in 200 mM PBS (pH = 7.0) along with the increase of hydrated particle size. In addition, when the RuDSNs were coated by the negative charged polymer (PSS), the zeta potential decreased dramatically. On the contrary, further coating RuDSNs@PSS with the positive charged polymer (PAH) made the zeta potential significantly increase. According to the change of the zeta potential and hydrated particle size, we ensured the successful modification of different capping agents. For the modification of the electrode surface, we used BSA, PAH, and PSS to block the GC electrode surface for obtaining different charges and steric hindrances. Abundant negatively charged groups (hydroxy, epoxy, and carboxyl) on GC electrode surface can adsorb positively charged PAH by strong electrostatic interaction, and then further adsorbed negatively charged PSS.

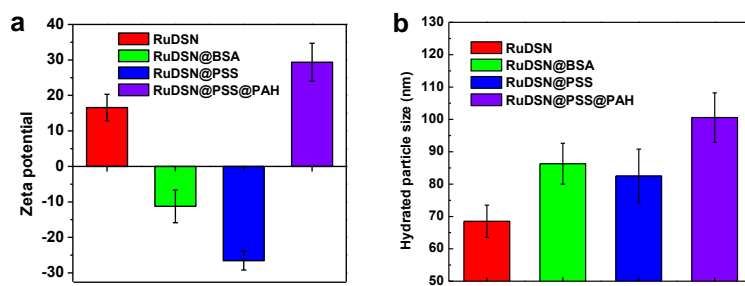


Figure S10. Zeta potential (a) and hydrated particle size (b) of bare RuDSNs, RuDSN@BSA, RuDSN@PSS, RuDSN@PSS@PAH.

Spatial distribution of collision intensity and frequency across GC electrode surface: We recorded the collision intensity and frequency across the electrode surface by adjusting the GC electrode holder on the mobile stage. Because the CCD view was too small to image the whole electrode surface, we recorded thirty adjoining regions along the equator of electrode surface (Figure S11). The collision frequency of the overall electrode surface can be obtained by the area integrated method.

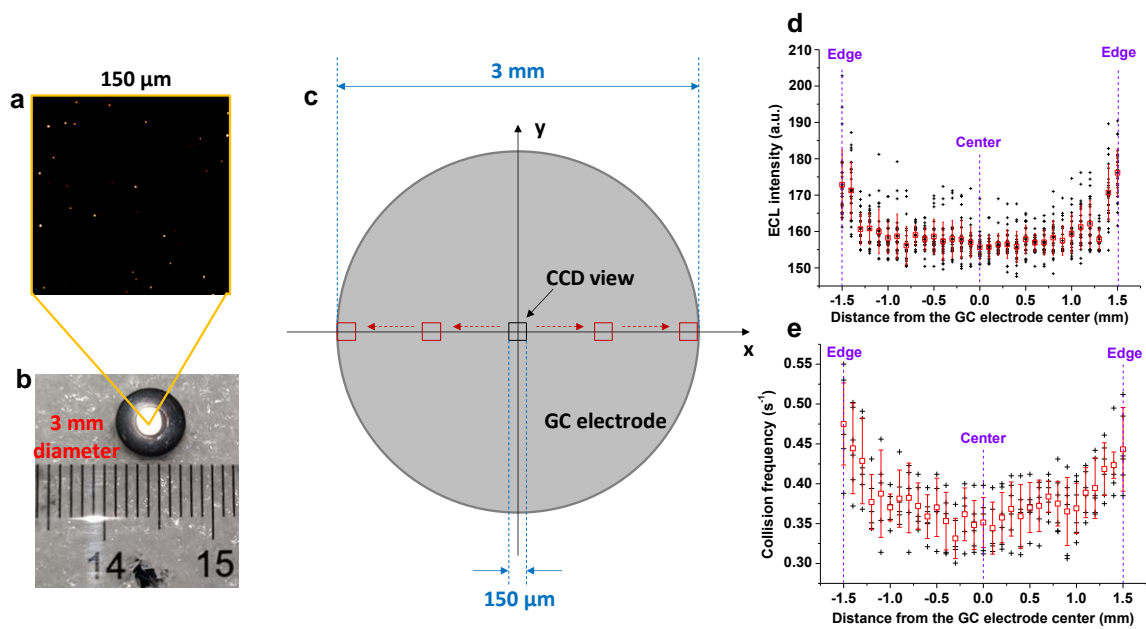


Figure S11. (a) Typical ECL image from the whole CCD-view (150 μm × 150 μm). (b) Photograph of the GC electrode used in our experiments. (c) Schematic diagram of relative size of the GC electrode and the CCD view. The squares represent the shifting CCD view from the center of electrode to the edge. (d) Statistic ECL intensity of transient collision vs distance from the center of the GC electrode. Black crosses represent the ECL intensity of each collision. (e) Statistic collision frequency vs distance from the center of the GC electrode. Black crosses represent the collision frequency in different regions. Red squares are data averaged to obtain the general trend. Error bars indicate the standard deviation. The position of GC electrode is finely adjusted by the mobile stage.

ECL intensity distribution of statistic sticking collision events in the CCD-view:

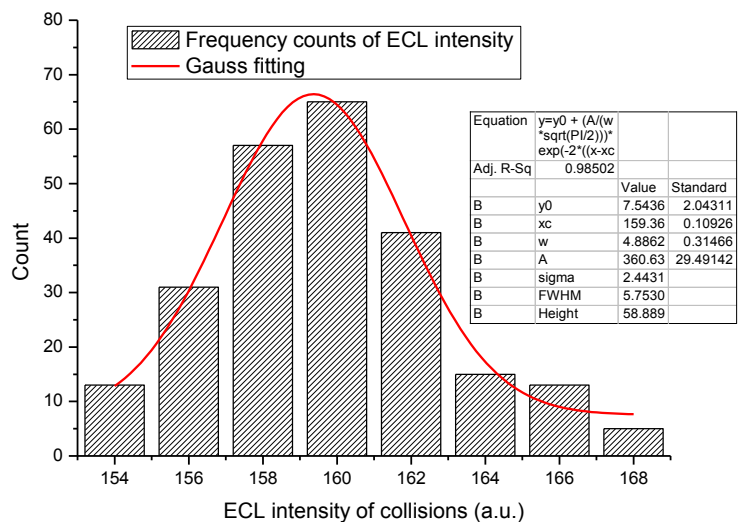


Figure S12. ECL intensity distribution of statistic sticking collision events in the CCD-view located in the center of GC electrode. Recording time: 1000 s.

Relay probe based on successive collision events: Because the PL intensity of single nanoparticle was directly proportional to the amount of doping $\text{Ru}(\text{bpy})_3^{2+}$ dyes in the 3D siloxane matrices, we imaged the PL intensity of a same set of RuDSNs before and after ECL imaging. Figure S13 showed that the PL intensity of RuDSNs decreased significantly after ECL reactions (Constant voltage: 1.4 V. Duration: 20 s). The PL intensity decayed too fast to be attributed to the leakage of $\text{Ru}(\text{bpy})_3^{2+}$ or photobleaching. As a result, it should be ascribed to the depletion of $\text{Ru}(\text{bpy})_3^{2+}$ inside nanoparticles during the ECL reactions.

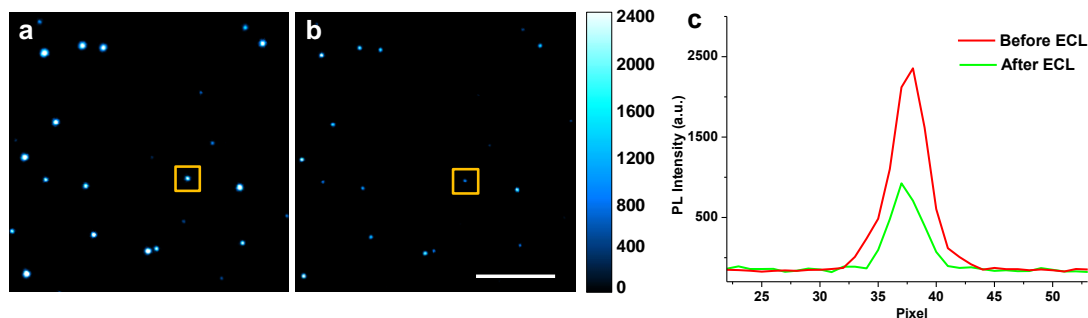


Figure S13. The PL images of a same set of RuDSNs on the GC electrode surface before (a) and after (b) the ECL imaging. (c) The PL intensity of the same RuDSN marked in (a) and (b). The constant potential: 1.4 V. Scale bars (white), 10 μm .

In collision experiments, the concentration of RuDSNs in the solution is very low (10 pM). Moreover, we notice that only those RuDSNs sticking to the electrode surface show rapid leakage of the $\text{Ru}(\text{bpy})_3^{2+}$ molecules inside RuDSNs, and these leaking $\text{Ru}(\text{bpy})_3^{2+}$ molecules then diffuse to the whole solution. We compare the ECL emission of RuDSNs and neighbouring area, and results reveal that the ECL background caused by the leaking $\text{Ru}(\text{bpy})_3^{2+}$ molecules is negligible (Figure S14).

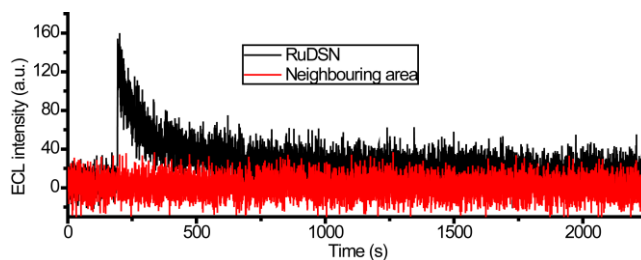


Figure S14. The ECL intensity-time curve of the RuDSN and the neighbouring blank area.

To perform the relay probe experiment, 80 μM CouMC (A H_2S -responsive molecule, Figure S15a) was added into the electrolyte (200 mM PBS buffer containing 100 mM TPA) before injecting RuDSNs. In the absence of H_2S , CouMC showed a significant absorbance at 589 nm, while RuDSNs showed a strong ECL emission at 619 nm (Figure S15b). Because of the overlap of the ECL emission and the absorption of CouMC, the collisional ECL intensity was quenched by CouMC, leading to a suppressed ECL spot from each collision at the beginning. On the contrary, when we added H_2S into the electrolyte, the reaction between H_2S and the indolenium C-2 atom of CouMC reduced the absorption of CouMC, and was completed within seconds. As a result, the ECL intensity of transient collisions from freshly sticking nanoparticles obviously increased when successively adding 20 μM H_2S into the electrolyte. The mean value of each plateau showed a linear relationship with the concentration of H_2S from 0 μM to 80 μM (Figure S16).

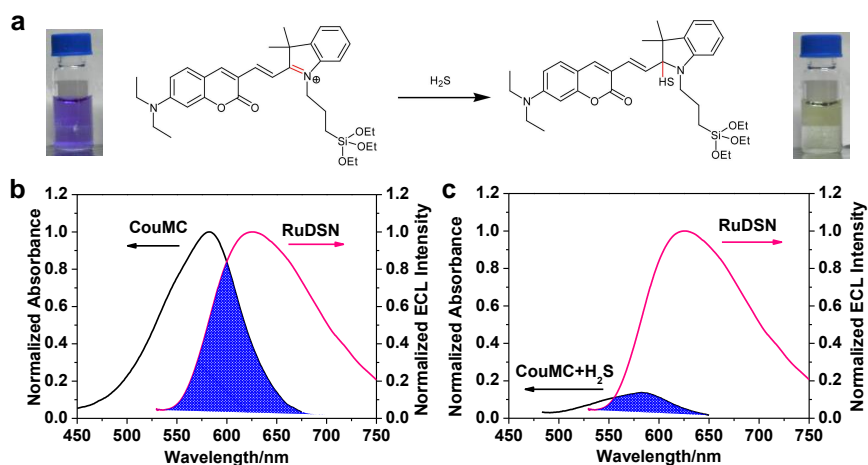


Figure S15. (a) The H_2S sensing mechanism of CouMC. Inset: the photograph of CouMC solution before and after adding H_2S . (b) Absorbance spectrum (black line) of CouMC in the absence (b) and presence (c) of H_2S . Pink line and blue grid line represent the ECL emission spectrum of RuDSNs and the overlap area, respectively.

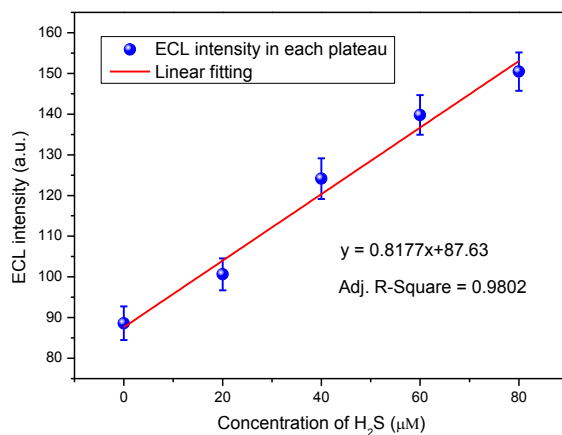


Figure S16. ECL intensity of statistic transient collision events at each plateau. The blue dots represent the average collision intensity at the present of 0, 20, 40, 60, 80 μM H_2S . Error bars indicate the standard deviation. The red line is the linear fitting curve.

6. COMSOL simulation for sub-particle ECL pattern analysis

Reactions and parameters for digital simulation:

Table S1. All reactions involving the ECL process.

Homogeneous reactions	$\text{TPAH}^+ \leftrightarrow \text{TPA} + \text{H}^+$	(1)
	$\text{BufH}^+ \leftrightarrow \text{Buf} + \text{H}^+$	(2)
	$\text{H}_2\text{O} \leftrightarrow \text{OH}^- + \text{H}^+$	(3)
	$\text{TPA}^{*+} - \text{H}^+ \xrightarrow{k_3} \text{TPA}^*$	(4)

Charge transfer reactions	$\text{TPA} - e \xrightarrow{k_{s2}} \text{TPA}^{*+}$	(5)
	$\text{TPA}^* - e \xrightarrow{k_{s4}} \text{P}_1$	(6)
Particle surface reactions	$ \text{-Ru}^{2+} + \text{TPA}^* \xrightarrow{k_4} \text{-Ru}^+ + \text{P}_1$	(7)
	$ \text{-Ru}^+ + \text{TPA}^{*+} \xrightarrow{k_5} \text{-Ru}^{2+*} + \text{TPA}$	(8)
	$ \text{-Ru}^{2+*} \xrightarrow{k_{des}} \text{-Ru}^{2+} + h\nu$	(9)

Table S2. Simulation parameters in global definitions.

Category	Name	Expression	Value	Description
Initial concentration	cTPrA0	0.1[mol/L]	100 mol/m ³	Initial concentration of TPA
	cTPrAH0	0.1[mol/L]	100 mol/m ³	Initial concentration of TPAH ⁺
	c0_Ru2	10 ⁻⁹ [mol/cm ²]	10 ⁻⁵ mol/m ²	The coverage rate of Ru(bpy) ₃ ²⁺
	cH0	10 ^{-7.4} [mol/L]	3.98*10 ⁻⁵ mol/m ³	Initial concentration of H ⁺
	cBuf0	0.2[mol/L]	200 mol/m ³	Initial concentration of PBS
Diffusion coefficient	DTPA	5*10 ⁻⁶ [cm ² /s]	5*10 ⁻¹⁰ m ² /s	Diffusion coefficient of TPA, TPA ⁺ and TPA [*]
	DRu	5*10 ⁻⁷ [cm ² /s]	5*10 ⁻¹¹ m ² /s	Diffusion coefficient of Ru(bpy) ₃ ²⁺
	DH	9.3*10 ⁻⁵ [cm ² /s]	9.3*10 ⁻⁹ m ² /s	Diffusion coefficient of H ⁺
	DBuf	5*10 ⁻⁶ [cm ² /s]	5*10 ⁻¹⁰ m ² /s	Diffusion coefficient of PBS
Reactions rate	k1	8 [1/s]	8 1/s	Forward rate constant for TPA generation (eq 1)
	k_1	3*10 ¹⁰ [L/mol/s]	3*10 ⁷ m ³ /(s·mol)	Backward rate constant for TPA generation (eq 1)
	kb	2*10 ³ [1/s]	2000 1/s	Forward rate constant for HPO ₄ ²⁻ generation (eq 2)
	k_b	3*10 ¹⁰ [L/mol/s]	3*10 ⁷ m ³ /(s·mol)	Backward rate constant for HPO ₄ ²⁻ generation (eq 2)
	ke	2*10 ⁻³ [1/s]	0.002 1/s	Forward rate constant for H ⁺ generation (eq 3)
	k_e	3*10 ¹⁰ [L/mol/s]	3*10 ⁷ m ³ /(s·mol)	Backward rate constant for H ⁺ generation (eq 3)
	k3	3500 [1/s]	3500 1/s	Rate constant for TPA [*] generation (eq 4)
	k4	3*10 ⁵ [L/mol/s]	300 m ³ /(s·mol)	Rate constant for Ru ⁺ generation on particle surface (eq 7)
	k5	3*10 ⁵ [L/mol/s]	300 m ³ /(s·mol)	Rate constant for Ru ^{2+*} generation on particle surface (eq 8)
	ks2	10 [cm/s]	0.1 m/s	Rate constant for TPA ⁺ generation on electrode surface (eq 5)
	ks4	10 [cm/s]	0.1 m/s	Rate constant for P ₁ generation on electrode surface (eq 6)
kdes	300 [1/s]	300 1/s	Rate constant for ECL generation on particle surface (eq 9)	
Particle sizes	d_bead	0.09, 0.42, 1.5 [μm]	9*10 ⁻⁸ , 4.2*10 ⁻⁷ , 1.5*10 ⁻⁶ m	The diameter of three sizes of RuCSPs
	r_bead	d_bead/2	4.5*10 ⁻⁸ , 2.1*10 ⁻⁷ , 7.5*10 ⁻⁷ m	The radius of three sizes of RuCSPs
	Dapp	0.1*DRu	5*10 ⁻¹² m ² /s	Apparent diffusion coefficient of Ru(bpy) ₃ ²⁺

Subdomain setting: Chemical reactions were introduced in the subdomain settings. The semicircle represented the RuCSP, whose surface was covered by Ru(bpy)₃²⁺ molecules. The rectangle represented the electrolyte, where the homogeneous chemical reactions occurred. The bottom edge represented the electrode surface, where charge transfer reactions occurred.

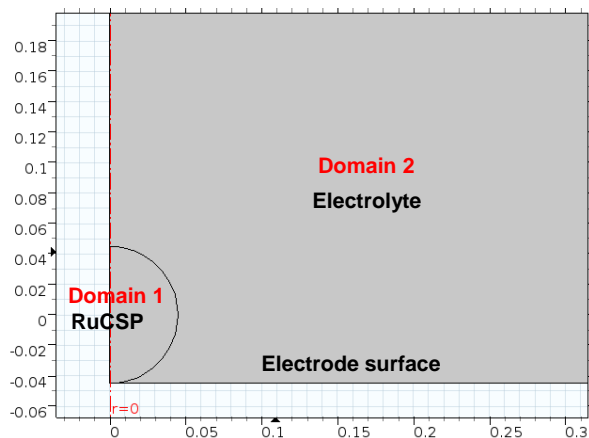


Figure S17. Geometry modeling of 90 nm RuCSP in COMSOL software. The 420 nm and 1.5 μm RuCSPs were conducted in the same manner.

Table S3. In the electrolyte (Entire model, domain 2), the concentration change of TPA, TPA⁺⁺ and TPA^{*} with time.

The concentration change of TPA	$\frac{\partial[\text{TPA}]}{\partial t} = D_{\text{sol}}\Delta[\text{TPA}] - k_1[\text{TPA}] + k_{-1}[\text{TPA}^*]$	(10)
The concentration change of TPA ⁺⁺	$\frac{\partial[\text{TPA}^{++}]}{\partial t} = D_{\text{sol}}\Delta[\text{TPA}^{++}] - k_3[\text{TPA}^{++}]$	(11)
The concentration change of TPA [*]	$\frac{\partial[\text{TPA}^*]}{\partial t} = D_{\text{sol}}\Delta[\text{TPA}^*] + k_3[\text{TPA}^{++}]$	(12)

Table S4. In the electrolyte (Entire model, domain 2), the reaction rates of TPA, TPA⁺⁺ and TPA^{*}.

Variables in the electrolyte	Expression	Unit	Description
R_TPA	$k_1 \cdot c_{\text{TPAH}}$	$\text{mol}/(\text{m}^3 \cdot \text{s})$	The generating rate of TPA in the electrolyte
R_TPA1	$k_3 \cdot c_{\text{TPA}^{++}}$	$\text{mol}/(\text{m}^3 \cdot \text{s})$	The generating rate of TPA [*] in the electrolyte
R_TPA2	$-k_3 \cdot c_{\text{TPA}^{++}}$	$\text{mol}/(\text{m}^3 \cdot \text{s})$	The generating rate of TPA ⁺⁺ in the electrolyte

Table S5. On the electrode surface (boundary), the concentration change of TPA, TPA⁺⁺, TPA^{*} and P₁.

The concentration change of TPA and TPA ⁺⁺	$D_{\text{sol}} \frac{\partial[\text{TPA}]}{\partial r} \Big _{\text{ele,surf}} = -D_{\text{sol}} \frac{\partial[\text{TPA}^{++}]}{\partial r} \Big _{\text{ele,suf}} = -k_{s2}[\text{TPA}]$	(13)
The concentration change of TPA [*] and P ₁	$D_{\text{sol}} \frac{\partial[\text{TPA}^*]}{\partial r} \Big _{\text{ele,surf}} = -D_{\text{sol}} \frac{\partial[\text{P}_1]}{\partial r} \Big _{\text{ele,suf}} = -k_{s4}[\text{TPA}^*]$	(14)

Table S6. On the electrode surface (boundary), the reaction rates of TPA, TPA⁺⁺, TPA^{*} and P₁.

Variables on the electrode surface	Expression	Unit	Description
R_TPA_e	$-k_{s2} \cdot c_{\text{TPA}}$	$\text{mol}/(\text{m}^2 \cdot \text{s})$	The generating rate of TPA on the electrode surface
R_TPA2_e	$k_{s2} \cdot c_{\text{TPA}}$	$\text{mol}/(\text{m}^2 \cdot \text{s})$	The generating rate of TPA ⁺⁺ on the electrode surface
R_TPA1_e	$-k_{s4} \cdot c_{\text{TPA}^*}$	$\text{mol}/(\text{m}^2 \cdot \text{s})$	The generating rate of TPA [*] on the electrode surface

R_P1_e	ks4*cTPA1	mol/(m ² *s)	The generating rate of P ₁ on the electrode surface
--------	-----------	-------------------------	--

Table S7. On the surface of three sizes of RuCSPs (90, 420, 1500 nm), the concentration change of Ru²⁺, Ru⁺, Ru²⁺, TPA, TPA⁺, TPA⁺ and P₁.

The concentration change of Ru ²⁺	$\frac{\partial \Gamma_{Ru^{2+}}}{\partial t} = D_{app,surf} \Delta \Gamma_{Ru^{2+}} - k_4 \Gamma_{Ru^{2+}} [TPA^*] + k_{des} \Gamma_{Ru^{2+}}$	(15)
The concentration change of Ru ⁺	$\frac{\partial \Gamma_{Ru^+}}{\partial t} = D_{app,surf} \Delta \Gamma_{Ru^+} + k_4 \Gamma_{Ru^{2+}} [TPA^*] - k_5 \Gamma_{Ru^+} [TPA^{++}]$	(16)
The concentration change of Ru ²⁺	$\frac{\partial \Gamma_{Ru^{2+}}}{\partial t} = D_{app,surf} \Delta \Gamma_{Ru^{2+}} + k_5 \Gamma_{Ru^+} [TPA^{++}] - k_{des} \Gamma_{Ru^{2+}}$	(17)
The concentration change of TPA and TPA ⁺	$D_{sol} \frac{\partial [TPA^{++}]}{\partial r} \Big _{p,surf} = -D_{sol} \frac{\partial [TPA]}{\partial r} \Big _{p,suf} = -k_5 \Gamma_{Ru^+} [TPA^{++}]$	(18)
The concentration change of TPA ⁺ and P ₁	$D_{sol} \frac{\partial [TPA^*]}{\partial r} \Big _{p,surf} = -D_{sol} \frac{\partial [P_1]}{\partial r} \Big _{p,suf} = -k_4 \Gamma_{Ru^{2+}} [TPA^*]$	(19)

Physical fields: Two physical fields were used for simulating ECL reactions. In “Transport of Diluted Species” physical field, time-dependent study on transport of diluted species was used to simulate the concentration around the RuDSNs. The inflow of the pristine substances to the electrode and the outflow of the products to the bulk solution were described below. For studying the concentration variation of both Ru(bpy)₃²⁺ and its derivatives on the RuDSNs surface, “Coefficient Form Boundary Partial Differential Equation” physical field was added into the model based on the electrode-electrolyte interface coupling.

Table S8. Variables and parameters in the added physics (the transport of diluted species in the chemical species transport).

The concentration of dependent variables	Domain	Diffusion efficient (m ² /s)	Initial concentration (mol/m ³)	Reaction rates (mol/(m ³ .s))	Inward flux (electrode surface boundary) (mol/(m ² .s))	Inward flux (particle boundary) (mol/(m ² .s))
cH	Electrolyte	DH	cH0	0		
cBuf	Electrolyte	DBuf	cBuf0	0		
cTPA	Electrolyte	DTPA	cTPA0	R_TPA	R_TPA_e	R_TPA_b
cTPAH	Electrolyte	DTPA	cTPAH0	0		
cTPA1	Electrolyte	DTPA	0	R_TPA1	R_TPA1_e	R_TPA1_b
cTPA2	Electrolyte	DTPA	0	R_TPA2	R_TPA2_e	R_TPA2_b
cP ₁	Electrolyte	DTPA	0	0	R_P1_e	R_P1_b
cBufH	Electrolyte	DBuf	cBuf0	0		

Table S9. On the surface of three sizes of RuCSPs (90, 420, 1500 nm), the reaction rates of Ru²⁺, Ru⁺, Ru²⁺, TPA, TPA⁺, TPA⁺ and P₁ via electrode-electrolyte interface coupling.

Variables on the particle surface	Expression	Unit	Description
R_Ru2_b	$-k_4 * c1_Ru2 * cTPA1 + k_{des} * c1_Ru2_1$	mol/(m ² *s)	The generating rate of Ru ²⁺ on the particle surface
R_Ru1_b	$k_4 * c1_Ru2 * cTPA1 - k_5 * c1_Ru1 * cTPA2$	mol/(m ² *s)	The generating rate of Ru ⁺ on the particle surface
R_Ru21_b	$k_5 * c1_Ru1 * cTPA2 - k_{des} * c1_Ru2_1$	mol/(m ² *s)	The generating rate of Ru ²⁺ on the particle surface
R_TPA_b	$k_5 * c1_Ru1 * cTPA2$	mol/(m ² *s)	The generating rate of TPA on the particle surface
R_TPA2_b	$-k_5 * c1_Ru1 * cTPA2$	mol/(m ² *s)	The generating rate of TPA ⁺ on the particle surface

R_TPA1_b	$-k_4 \cdot c_{1_Ru2} \cdot c_{TPA1}$	mol/(m ² ·s)	The generating rate of TPA' on the particle surface
R_P1_b	$k_4 \cdot c_{1_Ru2} \cdot c_{TPA1}$	mol/(m ² ·s)	The generating rate of P ₁ on the particle surface
i_TPA_b	R_TPA_b * F_const	A/m ²	The reaction current density of TPA on the particle surface
i_TPA2_b	R_TPA2_b * F_const	A/m ²	The reaction current density of TPA ⁺⁺ on the particle surface
i_TPA1_b	R_TPA1_b * F_const	A/m ²	The reaction current density of TPA' on the particle surface
i_P1_b	R_P1_b * F_const	A/m ²	The reaction current density of P ₁ on the particle surface

Table S10. Variables and parameters in another added physics (coefficient form boundary partial differential equation).

Dependent variables	Diffusion coefficient (particle surface boundary) (m ² /s)	Source term (mol/(m ² ·s))	Damping or mass coefficient	Initial values (mol/m ²)
c1_Ru2	Dapp	R_Ru2_b	1	c0_Ru2
c1_Ru1	Dapp	R_Ru1_b	1	0
c1_Ru2_1	Dapp	R_Ru21_b	1	0

Meshes settings: Because the geometry of the model was simple, the mesh setting was extremely fine.

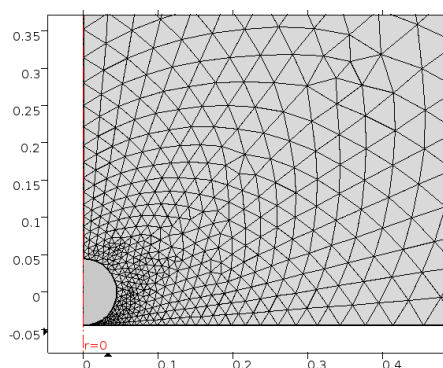


Figure S18. Mesh settings of 90 nm RuCSPs in COMSOL software. The 420 nm and 1.5 μm RuCSPs were conducted in the same manner.

Simulation results: The ECL intensity depended on the distance from the electrode surface (z axis). At large z, the ECL emission was controlled by the TPA⁺⁺ concentration that showed a decay trend with increasing distance from the electrode surface, according to the “revisited” route.

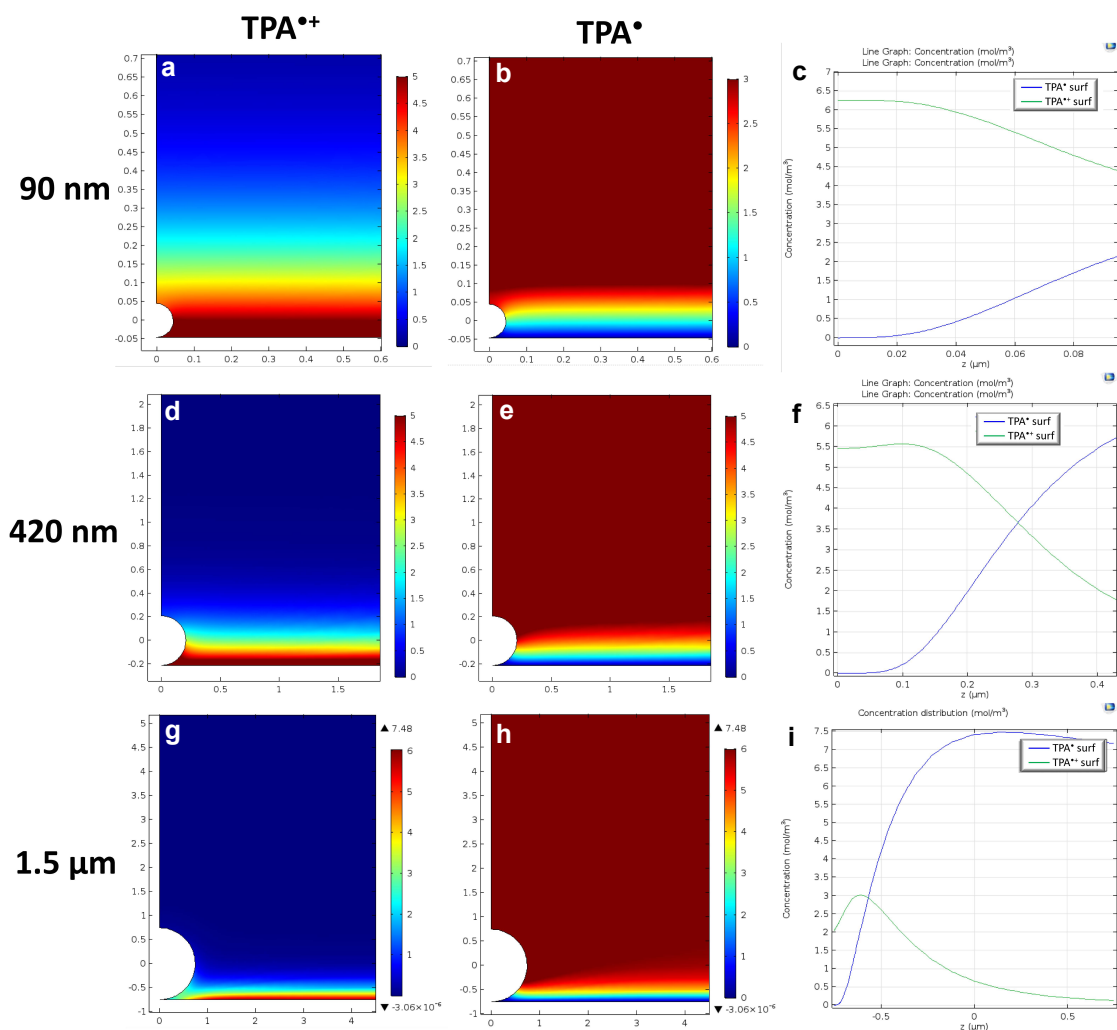


Figure S19. The side-view of steady state concentration pattern of TPA⁺ (a,d,g) and TPA[•] (b,e,h) on the three different RuCSPs surface. The plots of TPA⁺ and TPA[•] concentrations with increasing distance from electrode surface (c,f,i).

At small z , we must consider the electron tunnelling/hopping mechanism at the electrode surface. The electron tunnelling/hopping or lateral charge propagation was simulated by introducing an apparent surface diffusion ($D_{app,surf}$) of $Ru(bpy)_3^{2+}$ species.^[5] Therefore, by combining the revisited route with the electron tunnelling/hopping route, we simulated the ECL emission patterns of single RuCSPs (Figure S20).

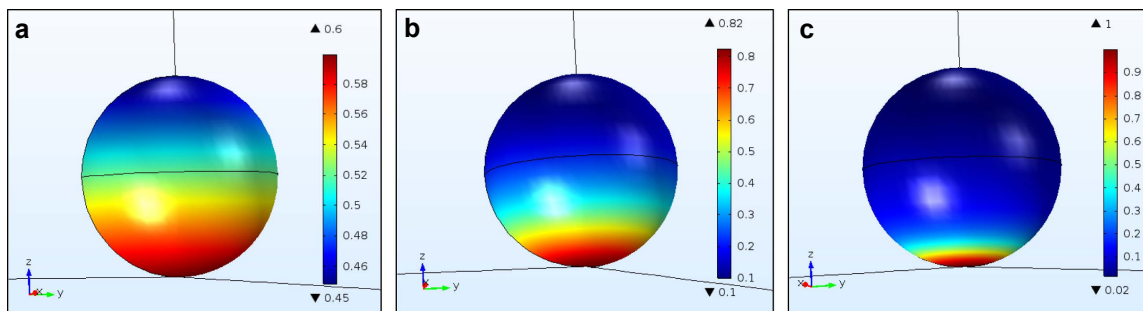


Figure S20. The 3D ECL emission pattern of (a) 90 nm RuCSP, (b) 420 nm RuCSP, and (c) 1.5 μm RuCSP in COMSOL software.

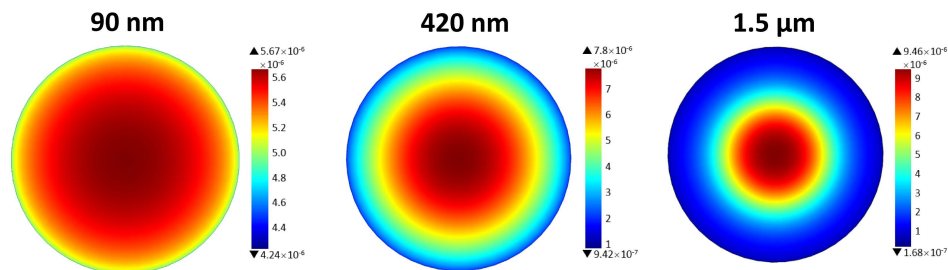


Figure S21. Bottom view of simulated ECL intensity distribution of three RuCSPs with different sizes.

As shown in Table S11, both experimental and simulated results showed that the ECL emission efficiency gradually decreased with the increasing particle sizes from 90 nm to 1.5 μm , suggesting that higher percentage of $\text{Ru}(\text{bpy})_3^{2+}$ dyes participated in the ECL reactions for smaller particles. The bottom view of the simulated ECL distribution also indicated that smaller particles showed more ECL emission areas (Figure S21), which underscored the superiority of nanoscale particles and offered valuable indications to design more efficient ECL nano-labels for ultrasensitive biosensors.

Table S11. The summary of the superficial area, PL intensity, and ECL intensity (experimental values and simulated values) of three RuCSPs.

Diameter (nm)	Superficial area ^[a]	PL ^[a]	ECL ^[a]	ECL efficiency ^[a]	Simulated ECL ^[a]	Simulated ECL efficiency ^[a]
90	1	1	1	100%	1	100%
420	21.8	27.3	14.2	65.1%	12.64	58.0%
1500	277.8	319.2	78.8	28.4%	86.98	31.3%

[a] Normalized by the 90 nm RuCSP.

7. Experimental section

Chemicals and general techniques: Tripropylamine (TPA), tris(2,2'-bipyridyl)dichlororuthenium(II) hexahydrate ($\text{Ru}(\text{bpy})_3^{2+}$), bis(2,2'-bipyridine)-4'-methyl-4-carboxybipyridine-ruthenium N-succinimidyl ester-bis(hexafluorophosphate) (Ru-NHS), 3-aminopropyltriethoxysilane (APTES), bovine serum albumin (BSA, $M_w \sim 66.43$ kDa), poly(allylamine hydrochloride) (PAH, $M_w \sim 50,000$), and poly(sodium 4-styrenesulfonate) (PSS, $M_w \sim 70,000$) were purchased from Sigma-Aldrich. 3-isocyanatopropyltriethoxysilane (ICP), N-(3-dimethylaminopropyl)-N'-ethylcarbodiimide hydrochloride (EDC) and N-hydroxysuccinimide (NHS) were purchased from Aladdin Reagent Inc. Bis(2,2'-bipyridyl)(2,2'-bipyridine-4,4'-dibutanoic acid)ruthenium(II) dichloride (Ru-COOH) was purchased from Suna Tech Inc. Polyethyleneimine (PEI, branched, M.W. 10000) was purchased from Alfa Aesar. Tetraethyl orthosilicate (TEOS) was purchased from Sinopharm Reagent (Beijing China). Sodium sulfide nonahydrate was purchased from Nanjing Chemical Reagent. Ultrapure water with a resistivity of 18.2 $\text{M}\Omega$ cm was produced using a Milli-Q apparatus (Millipore) and used in the preparation of all solutions. PDMS was prepared using Sylgard 184, Dow Corning. CouMC was synthesized according to the previous method.^[6]

Prior to use, GC and gold electrodes (3 mm in diameter) were polished sequentially with 0.3 and 0.05 μm alumina slurry on an abrasive cloth, followed by ultrasonic cleaning with ethanol and ultrapure water thoroughly. Then the electrodes were allowed to dry under a N_2 flow. The ECL spectrum of RuDSNs was collected by a homemade spectral acquiring system.^[6] The setup was comprised of a monochromator (Acton SP2300i, PI), a spectrograph CCD (PIXIS 400BR_excelon, PI), a grating (grating density: 300 L/mm; blazed wavelength: 500 nm), a CHI 660D electrochemical workstation, a cuvette holder and a light-tight cover. Scanning electron microscopy (SEM) micrographs were measured on a Model S-4800 scanning electron microscope. Transmission electron microscopy (TEM) micrographs were measured on a JEOL JEM 200CX transmission electron microscope, using an accelerating voltage of 100 kV. Ultraviolet-visible light (UV-vis) spectra were recorded on a Model UV-3600 spectrophotometer (Shimadzu, Kyoto, Japan). EIS analysis was carried out on an Autolab PGSTAT12 (Ecochemie, BV, The Netherlands) in EIS buffer with the frequency range of 10^{-1} to 10^5 Hz, 5 mV amplitude. Electrochemical

measurements were performed on a CHI 660D workstation (CH Instruments Inc., Shanghai, China). The zeta potential was tested on a Nano-z zeta potential analyzer. Dynamic light scattering (DLS) experiments were performed at 25 °C using a Brookhaven BI-200SM instrument, equipped with a He-Ne laser (632.8 nm) at a fixed scattering angle of 90 °.

Preparation and characterization of RuDSNs and RuCSPs:

62 nm RuDSNs:^[7] 1.77 mL of Triton X-100 was added into 7.5 mL of cyclohexane and 1.8 mL of *n*-hexanol. After 10 min of stirring, 340 μL of 0.04 M Ru(bpy)₃²⁺ aqueous solution was added into the solution, followed by the addition of 100 μL TEOS. After a 5 min equilibration time, 60 μL NH₃·H₂O was added into the mixture to trigger the polymerization reaction. The reaction was left for 24 h at 25°C under mild stirring. Then, 2 mL of acetone was added and the solution was sonicated to break the emulsion. The precipitation was washed to remove the residual surfactant molecules and extra Ru(bpy)₃²⁺.

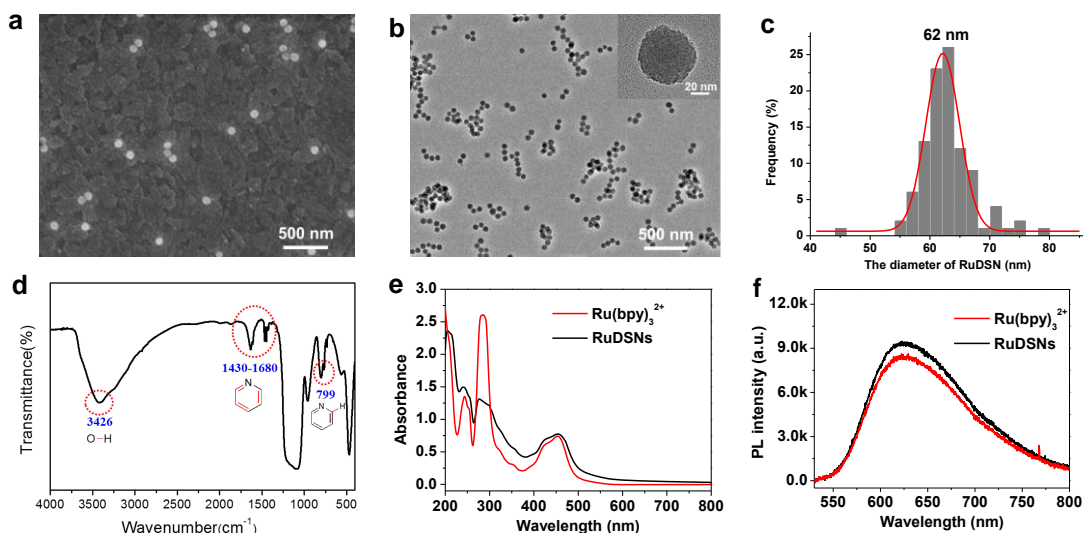


Figure S22. Characterization of RuDSNs (62 nm). SEM image (a) and TEM image (b) of RuDSNs sample. Inset in (b): the high resolution TEM image of single RuDSN. (c) The statistic sized distribution of RuDSNs. (d) The FT-IR analysis of RuDSNs. (e) The absorption spectra of Ru(bpy)₃²⁺ and RuDSNs. (f) The PL spectra of Ru(bpy)₃²⁺ and RuDSNs.

We synthesized RuDSNs for high ECL emission efficiency in aqueous solution. Incorporation of abundant Ru(bpy)₃²⁺ molecules inside the silica nanoparticle provided a great enhancement of the ECL emission. TEM and SEM images illustrated that RuDSNs had a spherical shape with a narrow distribution of diameter at 62 nm (Figure S22). The FT-IR spectrum showed the stretching vibration of the C=N (1430 cm⁻¹ to 1680 cm⁻¹) and C-H (799 cm⁻¹) in pyridine ring, suggesting the successful doping of Ru(bpy)₃²⁺ into the 3D siloxane matrices. Moreover, the absorption and PL spectra of RuDSNs was in accord with of Ru(bpy)₃²⁺, further confirming the successful doping. The doping amount of Ru(bpy)₃²⁺ molecule per RuDSN was estimated by the following equation.

$$n_{dye/NP} = \frac{c_{dye}}{c_{NP}} \quad (11)$$

where c_{dye} is the concentration of Ru(bpy)₃²⁺ in the RuDSNs solution, which is obtained by quantitative absorption spectra between Ru(bpy)₃²⁺ molecule solution and RuDSNs solution. $n_{dye/NP}$ is the doping amount of Ru(bpy)₃²⁺ molecule per RuDSN. c_{NP} is the concentration of RuDSNs, which can be obtained by the following equation.

$$c_{NP} = \frac{m_{bulk}}{m_{NP}N_A V_s} \quad (12)$$

where m_{bulk} is the mass of bulk RuDSNs. V_s is the volume of bulk RuDSNs solution. N_A is Avogadro's number. m_{NP} is the mass of single RuDSN, which is estimated by the following equation.

$$m_{NP} = \frac{4}{3}\pi r^3 \times \delta_{NP} \quad (13)$$

where δ_{NP} is the silica density (~2.2 g/mL). r is the average radius of RuDSNs (~31 nm). According to Eq. (1-3), we have that $n_{dye/NP} \approx 8854$.

500 nm RuDSNs: APTES (5 μL) and Ru-NHS (5 mg) were added to dry DMF (100 μL). The reaction mixture

was stirred for 1 h at room temperature. Then, the mixture was added into 2 mL dry ethanol, followed by the addition of 20 μL TEOS. The mixed solution was injected dropwise into 7 mL dry ethanol solution that contains 420 nm SiO_2 (20 mg) and 100 μL NH_4OH . After stirring for 16 h at 35°C, the as-prepared RuDSNs was collected by centrifugation at 5000 rpm and washing with water several times.

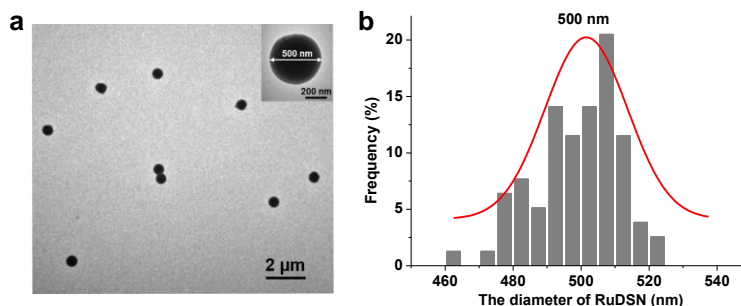


Figure S23. Characterization of RuDSNs (500 nm). (a) TEM image of RuDSNs with a zoom-in inset. (b) The statistic sized distribution of RuDSNs.

The preparation of the RuCSPs consisted of three steps: synthesis of $\text{Ru}(\text{bpy})_3^{2+}$ bonded PEI polymer, modification of the ICP group on the SiO_2 surface, and preparation of the RuCSPs.

Synthesis of $\text{Ru}(\text{bpy})_3^{2+}$ bonded PEI polymer. The following reagents were mixed in a flask: 2.1 mg PEI, 39.8 mg Ru-COOH , 38.3 mg EDC, 23 mg NHS and 2 mL 100 mM PBS (pH 7.4). The reaction solution was left overnight at room temperature under mild stirring. The crude product was purified by dialysis to yield $\text{Ru}(\text{bpy})_3^{2+}$ bonded PEI polymer.

Modification of the ICP group on the SiO_2 surface. 100 mg SiO_2 particles (90 nm, 420 nm and 1.5 μm) was dispersed in 25 mL anhydrous toluene, followed by the addition of 75 μL ICP. The mixture was stirring for 20 h under fierce reflux in N_2 atmosphere. The products were centrifuged and the precipitation was washed three times with ethanol to obtain ICP-modified SiO_2 .

Preparation of the RuCSPs. 1 mg ICP-modified SiO_2 (90 nm, 420 nm and 1.5 μm) was added into 1 mL PBS (100 mM, pH 7.4) solution of $\text{Ru}(\text{bpy})_3^{2+}$ bonded PEI polymer (1 mg/mL). This mixture was left overnight at room temperature under mild stirring. The excess $\text{Ru}(\text{bpy})_3^{2+}$ bonded PEI polymers were removed by centrifuging and washing with ethanol and water several times. The RuCSPs was redispersed in 1 mL distilled water.

8. Descriptions of the movies

Movie S1. ECL imaging of four immobilized RuDSNs during a CV scanning. (Potential: 0-1.4 V vs. Ag/AgCl , scan rate: 0.02 V/s, exposure time: 500 ms, electrolyte: 200 mM PBS, pH 7.4, containing 100 mM TPA).

Movie S2. ECL imaging of 3D motion trajectory during an elastic collision. (Constant potential: 1.4 V vs. Ag/AgCl , exposure time: 200 ms, electrolyte: 200 mM PBS, pH 7.4, containing 100 mM TPA).

Movie S3. ECL imaging of simultaneous sticking collisions of three nanoparticles. (Constant potential: 1.4 V vs. Ag/AgCl , exposure time: 200 ms, electrolyte: 200 mM PBS, pH 7.4, containing 100 mM TPA).

Movie S4. ECL imaging of relay probes based on successive collision events. (Constant potential: 1.4 V vs. Ag/AgCl , exposure time: 200 ms, electrolyte: 200 mM PBS, pH 7.4, containing 100 mM TPA and 80 μM CuMC . 20 μM H_2S was added each time).

9. Reference

- [1] Y. Zu, A. J. Bard, *Anal. Chem.* **2000**, *72*, 3223-3232.
- [2] a) K. Imai, G. Valenti, E. Villani, S. Rapino, E. Rampazzo, M. Marcaccio, L. Prodi, F. Paolucci, *J. Phys. Chem. C* **2015**, *119*, 26111-26118; b) M. Sentic, M. Milutinovic, F. Kanoufi, D. Manojlovic, S. Arbault, N. Sojic, *Chem. Sci.* **2014**, *5*, 2568-2572; c) W. Miao, J. P. Choi, A. J. Bard, *J. Am. Chem. Soc.* **2002**, *124*, 14478-14485; d) G. Valenti, S. Scarabino, B. Goudeau, A. Lesch, M. Jovič, E. Villani, M. Sentic, S. Rapino, S. Arbault, F. Paolucci, N. Sojic,

- J. Am. Chem. Soc.* **2017**, *139*, 16830-16837.
- [3] Z. F. Chen, Y. B. Zu, *J. Phys. Chem. C* **2008**, *112*, 16663-16667.
- [4] a) S. Zanarini, E. Rampazzo, L. D. Ciana, M. Marcaccio, E. Marzocchi, M. Montalti, F. Paolucci, L. Prodi, *J. Am. Chem. Soc.* **2009**, *131*, 2260-2267; b) G. Valenti, E. Rampazzo, S. Bonacchi, L. Petrizza, M. Marcaccio, M. Montalti, L. Prodi, F. Paolucci, *J. Am. Chem. Soc.* **2016**, *138*, 15935-15942.
- [5] a) C. Amatore, Y. Bouret, E. Maisonhaute, J. I. Goldsmith, H. D. Abruna, *Chem. Eur. J.* **2001**, *7*, 2206-2226; b) C. P. Andrieux, J. M. Savéant, *J. Electroanal. Chem.* **1980**, *111*, 377-381; c) W.-Y. Lee, M. Majda, G. Brezesinski, M. Wittek, D. Möbius, *J. Phys. Chem. B* **1999**, *103*, 6950-6956.
- [6] C. Ma, W. Wu, Y. Peng, M. X. Wang, G. Chen, Z. Chen, J. J. Zhu, *Anal. Chem.* **2018**, *90*, 1334-1339.
- [7] L. H. Zhang, S. J. Dong, *Anal. Chem.* **2006**, *78*, 5119-5123.